ACS APPLIED MATERIALS & INTERFACES

MOF-Derived Porous Co/C Nanocomposites with Excellent Electromagnetic Wave Absorption Properties

Yinyun Lü, Yiting Wang, Hongli Li, Yuan Lin, Zhiyuan Jiang, Zhaoxiong Xie, Qin Kuang,* and Lansun Zheng

State Key Laboratory for Physical Chemistry of Solid Surfaces & Department of Chemistry, College of Chemistry and Chemical Engineering, Xiamen University, Xiamen 361005, China

Supporting Information

ABSTRACT: Composites incorporating ferromagnetic metal nanoparticles into a highly porous carbon matrix are promising as electromagnetic wave absorption materials. Such special composite nanomaterials are potentially prepared by the thermal decomposition of metal−organic framework (MOF) materials under controlled atmospheres. In this study, using Co-based MOFs (Co-MOF, ZIF-67) as an example, the feasibility of this synthetic strategy was demonstrated by the successful fabrication of porous Co/C composite nanomaterials. The atmosphere and temperature for the thermal decomposition of MOF precursors were crucial factors for the formation of the ferromagnetic metal nanoparticles and carbon matrix in the porous Co/C composites. Among the three Co/C composites obtained at different temperatures, Co/C-500 obtained at 500 °C exhibited the best performance for electromagnetic wave absorption. In particular, the maximum reflection loss (RL) of Co/C-500 reached −35.3 dB, and the effective absorption bandwidth (RL ≤ −10 dB) was 5.80 GHz (8.40 GHz−14.20 GHz) corresponding to an absorber thickness of 2.5 mm. Such excellent electromagnetic wave absorption properties are ascribed to the synergetic effects between the highly porous structure and multiple components, which significantly improved impedance matching.

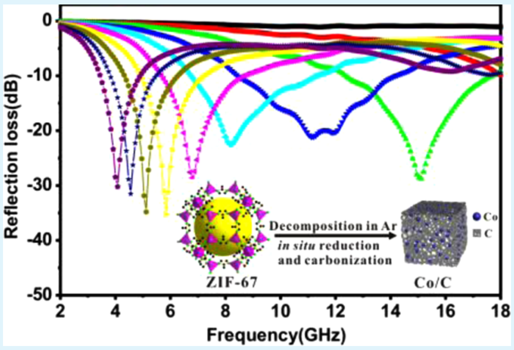

KEYWORDS: *metal−organic frameworks, self-sacrificial template synthesis, porous structure, Co/C composite, electromagnetic wave absorption*

1. INTRODUCTION

Electromagnetic waves have been widely used in various fields, such as scientific research, industrial production, as well as daily life. However, electromagnetic radiation causes environmental and health problems, such as the interference to the normal operation of electronic devices as well as harm to human bodies, which are becoming increasingly serious.[1−3] To address these problems, significant efforts have been devoted in past decades toward exploring high-efficiency electromagnetic wave absorption materials that are usually required to be lightweight, as well as exhibit strong absorption, high thermal stability, and a broad absorption frequency bandwidth.

Several materials such as ferrites, metals, carbons and conducting polymers can be applied for electromagnetic wave absorption, but they possess both advantages and disadvantages when applied alone.[4−7] For example, ferromagnetic metals such as Fe, Co and Ni as well as their alloys exhibit strong absorption intensity, whereas their frequency ranges are usually narrow.[8−11] In contrast, carbon-based materials such as carbon nanofibers, carbon nanotubes and graphene are good light-weight dielectric absorbers.[12,13] Previous studies have demonstrated that by the incorporation of ferromagnetic metallic nanoparticles into carbon-based materials, the values of dielectric permittivity and magnetic permeability of the resulting composite materials can be altered to achieve the maximal absorption of electromagnetic energy in a wide frequency range while significantly reducing their weight.[14−16] Hence, it can be observed that multielement composites are preferred as effective electromagnetic wave absorption materials. Notably, to achieve high performance in electromagnetic wave absorption, the organization architecture as well as the constituent of materials need to be rationally optimized. Typically, porous architectures, which are actually complex systems involving elastic structures and air cavities, with good properties such as low density and high specific surface, are conducive for improving the electromagnetic wave absorption performance of materials.[17−20] Nevertheless, it is still a significant challenge to achieve deliberate control over the constituent and architecture of porous materials in a simple and efficient manner.

Metal−organic framework (MOF) materials, which are mostly composed of metal−oxygen coordinating clusters as secondary building units and aromatic organic linkers, have been recently proven to be ideal templates for fabricating

Received: April 14, 2015
Accepted: June 3, 2015
Published: June 3, 2015

DOI: 10.1021/acsami.5b03177
ACS Appl. Mater. Interfaces 2015, 7, 13604−13611

various inorganic functional materials.[21] The most attractive advantages of this synthetic strategy based on the thermal decomposition of MOFs are that the as-formed materials are highly porous, and more importantly, the constituent of materials can be altered to metal, metal oxide, carbon or their hybrids in a facile manner by controlling the thermal decomposition conditions of MOFs.[22−26] Herein, taking Co-based MOFs as an example, we attempted to illustrate that this synthetic strategy has significant potential for fabricating composites of ferromagnetic metal nanoparticles and carbon with a highly porous structure. Fortunately, porous Co/C composite nanomaterials were successfully fabricated by the thermal decomposition of ZIF-67, a zeolitic imidazolate framework (ZIF)-type cobalt-containing MOF, under inert atmosphere. As we expected, the as-prepared porous Co/C composites exhibited significantly good performance for electromagnetic wave absorption.

2. EXPERIMENTAL SECTION

2.1. Chemicals. Cobalt nitrate hexahydrate ($Co(NO_3)_2{\cdot}6H_2O$, 99%), 2-methylimidazole (mIM, 99%), methanol (99.9%), and ethanol (99.7%) were obtained commercially (Alfa Aesar and Sinopharm Chemical Regent Co., Ltd.). All reagents were used without further purification.

2.2. Synthesis of Samples. Porous Co/C composites were prepared by the calcination of Co-based MOF (ZIF-67) precursors under Ar. The ZIF-67 precursors were prepared by the simple precipitation of $Co(NO_3)_2$ and mIM in a methanol solution at room temperature.[27] Typically, a 3 mL methanol solution of $Co(NO_3)_2{\cdot}6H_2O$ (0.50 mol dm^{-3}) was mixed with a 20 mL methanol solution of mIM (3.4 mol·dm^{-3}) and stirred for 6 h at room temperature. The resulting purple precipitate was collected by centrifugation, washed with alcohol for three times, and dried at 80 °C for 24 h. Then, the as-prepared Co-MOF (ZIF-67) precursors were loaded in a combustion boat and were heated at a rate of 5 °C·min^{-1} and maintained at 500−800 °C for 5 h under Ar. The as-synthesized products were denoted as Co/C-500, Co/C-600, and Co/C-800, based on the applied calcination temperatures.

2.3. Characterization of Samples. The morphologies of the samples were observed using scanning electron microscope (SEM, Hitachi S4800) and transmission electron microscope (TEM, JEOL 2010F) at an accelerating voltage of 200 kV. The phases of the samples were determined by X-ray powder diffraction (XRD) patterns recorded on a Rigaku D/max X-ray diffractometer (Cu Kα radiation, λ = 0.15418 nm). Raman spectra were measured on a Renishaw inVia Raman microscope with an argon ion laser with an excitation of 633 nm. The laser power was 10 mW, and the spot size was 2 mm. Thermogravimetry (TG) curves of the Co-MOF precursors were recorded on an SDT Q600TGA thermal gravimetric analyzer under N_2 or air in the temperature range of 30−900 °C with a heating rate of 10 °C min^{-1}. Element contents of the samples were determined using an Elementar Vario EL III instrument. Nitrogen adsorption−desorption isotherms were measured at 77 K on a Tristar II 3020 sorption analyzer (Micromeritics), and the specific surface area was determined by the Brunauer−Emmett−Teller (BET) method. The static magnetic properties of the as-prepared porous Co/C composites were measured by a Lake Shore 7404 vibrating sample magnetometer (VSM) at room temperature.

2.4. Electromagnetic Wave Absorption Measurements. For electromagnetic wave absorption measurements, the as-prepared porous Co/C composites were grinded with paraffin wax. To ensure well dispersion of Co/C abserbates, the content of paraffin wax was optimized and finally fixed to 40 wt %. And then the resulting abserbates/paraffin composites were compressed into cylindrical specimens with an inner diameter of 3 mm, outer diameter of 7 mm, and thickness of 2.5−3.5 mm. The complex permittivity ($\varepsilon_r = \varepsilon' - j\varepsilon''$) and relative complex permeability ($\mu_r = \mu' - j\mu''$) were determined using the T/R coaxial line method in the range of 2−18 GHz using a network analyzer (Agilent Technologies N5222A). The reflection loss (RL) curves calculated from the relative permeability and permittivity at the given frequency and absorber thickness were employed to evaluate the electromagnetic wave absorption properties.[28] The RL was calculated according to following equations

$$Z_{in} = Z_0(\mu_r/\varepsilon_r)^{1/2}\tanh[j(2\pi fd/c)(\mu_r\varepsilon_r)^{1/2}] \quad (1)$$

$$RL = 20\log|(Z_{in} - Z_0)/(Z_{in} + Z_0)| \quad (2)$$

where f is the frequency of the electromagnetic wave, d is the thickness of absorber, c is the velocity of light, μ_r and ε_r are the relative complex permeability and permittivity, respectively, Z_0 is the impedance of free space, and Z_{in} is the input impedance of the absorber.

3. RESULTS AND DISCUSSION

Figure 1a−c show the representative SEM and TEM images of the precursors: the precursors are clearly composed of submicrosized crystals having a rhombic dodecahedral morphology. As shown in the powder XRD pattern in Figure 1d, the precursors are pure ZIF-67, a type of Co-based MOFs, having sodalite topology with a unit cell containing two mIM linkers per cobalt ($Co(mIM)_2$).

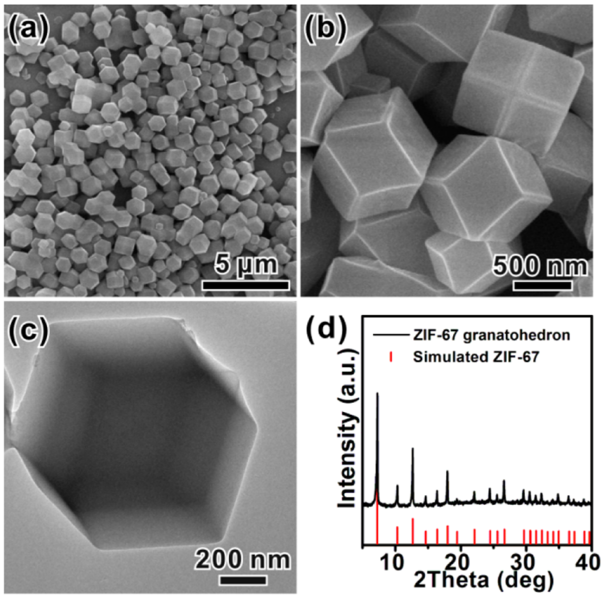

Figure 1. (a) Low-magnification and (b) high-magnification SEM images of Co-MOF (ZIF-67) precursors. (c) TEM image of an individual Co-MOF (ZIF-67) particle and (d) XRD pattern of the Co-MOF (ZIF-67) precursors.

Previous studies have demonstrated that porous nanostructures of metal, metal oxides, carbon or their hybrids can be converted from MOF precursors by thermal decomposition, depending on calcination conditions (e.g., atmosphere, temperature and time).[22−26] For preparing porous Co/C composites, the primary task clearly involves the use of appropriate atmosphere and temperature with regard to ZIF-67. Figure 2 shows the TG curves of the ZIF-67 precursors recorded under air and inert gas (N_2). By comparison of the two curves, ZIF-67 is more stable in N_2 than in air. In air, the decomposition of ZIF-67 starts around 300 °C and ends at 410 °C, and the total weight loss in this process is ~62.5%, which is very close to the theoretical value (63.7%) of the transformation from ZIF-67 to Co_3O_4.[29] However, in N_2, ZIF-67 is stable up to 400 °C. With increasing temperature, the weight of ZIF-67 sharply decreases

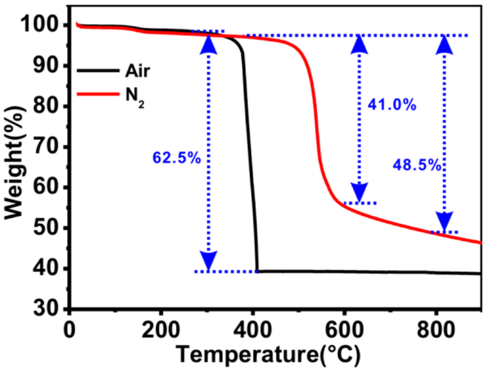

Figure 2. TG curves of the Co-MOF (ZIF-67) precursors under air and N_2.

at 500 °C and then continuously decreases with a relatively slow slope after 600 °C. The total weight loss in decomposition from 400 to 600 °C is ~41.0%, which is significantly lower than the theoretical values in the transformation from ZIF-67 to metallic Co (73.3%) or its oxides (63.7% for Co_3O_4 and 66.1% for CoO). This result implies that some carbon-containing materials are generated in the thermal decomposition of ZIF-67 under inert atmosphere, together with metallic Co or its oxides.

In the thermal decomposition of MOFs under inert atmosphere, organic components of MOFs can be directly carbonized and metal ions are reduced in situ, thereby forming metal/carbon hybrids. However, even a small amount of oxygen in the atmosphere during thermal decomposition would lead to the preferential formation of metal oxides in the products. This scenario has been completely demonstrated in our experiments (Figure S1 in the Supporting Information). To avoid this situation, we specifically conducted the thermal decomposition of Co-MOF (ZIF-67) precursors under a flow of extra pure (99.99%) Ar.

Figure 3a$_{1-3}$ shows typical SEM images of Co/C-500, Co/C-600, and Co/C-800, which are the products obtained at 500, 600, and 800 °C under Ar flow for 5 h, respectively. The particles of Co/C-500 and Co/C-600 roughly maintain their original rhombic dodecahedral shape, while the particle faces are concave, and the particle sizes significantly shrink because of the loss of organic components. In the corresponding low-magnification TEM images shown in Figure 3b$_{1-3}$, the particles in all samples are composed of primary crystallites with small sizes. Compared to Co/C-500, Co/C-600 looks looser, whereas Co/C-800 exhibits severe collapse. High-magnification TEM images shown in Figure 3c$_{1-3}$ reveal that these primary crystallites with dark contrast are supported by a carbon matrix, and the size of crystallites increases with calcination temperature. The average sizes of primary crystallites are ~6 nm for Co/C-500, ~10 nm for Co/C-600, and ~20 nm for Co/C-800. Such a porous structure of the samples was further confirmed by nitrogen adsorption−desorption analysis. The three samples display a typical type-IV isotherm with an H4-type hysteresis loop at a relative pressure of 0.4−0.9, which indicates the presence of a mesoporous structure (Figure S2 in the Supporting Information). Interestingly, as shown in Table 1, the specific surface areas of the three samples just fluctuate in the narrow range of 200−250 $m^2\ g^{-1}$ (204.7 $m^2\ g^{-1}$ for Co/C-500, 249.8 $m^2\ g^{-1}$ for Co/C-600, and 234.3 $m^2\ g^{-1}$ for Co/C-800). The impact of calcination temperature on specific surface areas of products mainly come from two aspects as below. Increasing calcination temperature is conducive to the carbonation of precursors, which has been proved by the element analysis (Table 1, C%: 33% for 500 °C and 37% for 800 °C). On the other hand, increasing calcination temperature will prompt the growth of Co nanoparticles, leading to the decrease of their surface area. Therefore, it is a result of comprehensive function of two above factors that Co/C-600 possesses the largest specific surface area among three samples. Note that, unlike the present case, the specific surface area significantly decreases with increasing calcination temperature for porous Co_3O_4 nanocages prepared by the thermal decomposition of ZIF-67 in air.[29] By the analysis of the above-mentioned opposite results, it is reasonable to conclude that the carbon matrix is formed in the products obtained under inert atmosphere, which prevents the further growth of metal primary crystallites to a certain extent.

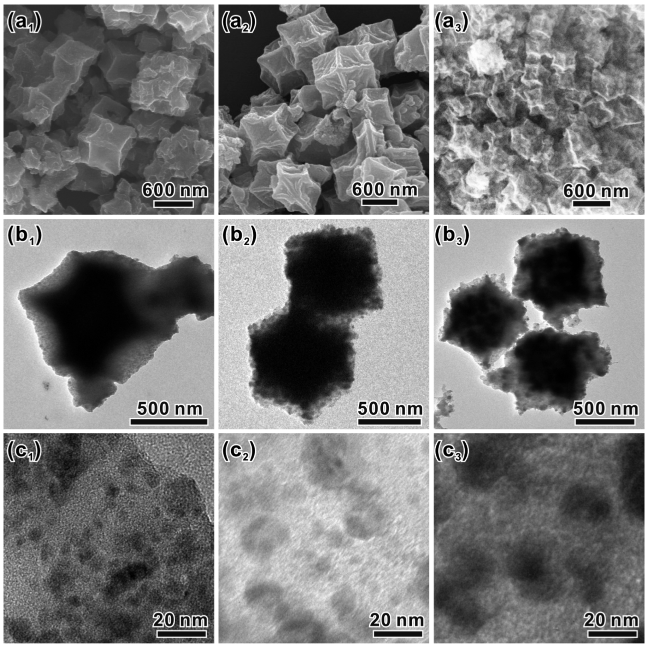

Figure 3. (a) Low-magnification SEM, (b) low-magnification TEM, and (c) high-magnification images of (1) Co/C-500, (2) Co/C-600, and (3) Co/C-800 obtained after calcination at different temperatures under Ar for 5 h.

Table 1. Specific Surface Areas and Element Analysis Results of Co/C-500, Co/C-600 and Co/C-800

			element analysis	
samples	T (°C)	S_{BET} ($m^2\ g^{-1}$)	C (%)	N (%)
Co/C-500	500	204.7	33.3	11.0
Co/C-600	600	249.8	33.0	6.1
Co/C-800	800	234.3	37.2	1.5

To ascertain the constituents of the samples, powder XRD analysis was further conducted. As shown in Figure 4a, the diffraction peaks are less resolved in Co/C-500, but they become increasingly stronger with increasing calcination temperature. This indicates that the high-temperature samples exhibit better crystallinity. In addition, they exhibit similar XRD features with a weak, broad peak at approximately 25°, in spite of poor background due to strong X-ray fluorescence of elemental Co under irradiation of monochrome Cu−Kα, which may be attributed to the (002) peak of graphitic carbon materials with a low degree of graphitization.[30] Besides this peak, three main peaks are observed at 44.2, 51.5, and 75.9°,

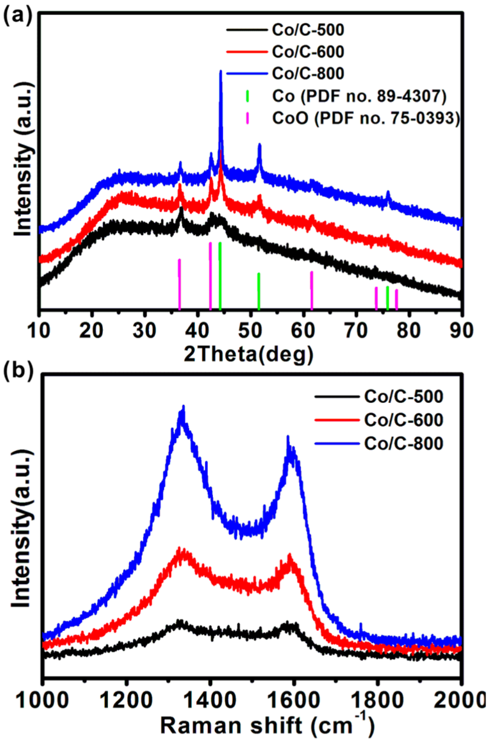

Figure 4. (a) XRD patterns and (b) Raman spectra of the three porous Co/C composites prepared at different temperatures under Ar.

which are attributed to the metallic Co of the *fcc* structure (PDF no. 89−4307). Moreover, some weak peaks assigned to CoO are also observed for the three samples, which are attributed to the oxidation of small Co nanoparticles during the exposure of the samples to air. A similar phenomenon has been reported previously.[31]

The presence of C in the products was also demonstrated by element analysis. As listed in Table 1, the C content in the as-prepared Co/C composites is around 33−37%, which is significantly higher than the normal value (∼2%) obtained for the thermal decomposition products obtained in air.[29] More detailed structural information about the chemical speciation of carbon was provided by Raman spectroscopy analysis. As shown in Figure 4b, the G band at ∼1590 cm^{-1} and the D band at ∼1330 cm^{-1} are clearly detected in the Raman spectra of the three Co/C composites. The G band is a characteristic feature of graphitic layers, whereas the D band corresponds to disordered carbon or defective graphitic structures. Interestingly, for the three samples, the integrated intensity ratios (I_D/I_G) for the D and G bands are constant around 1.1. This indicates that the three samples probably contain long-range disordered graphitic carbon, which is well consistent with weak and broad diffraction features at 25° in the XRD patterns. In addition, the higher the calcination temperature, the stronger the peak intensity. This indicates that the crystallization degree of carbon becomes better with temperature.

All results, when combined together, have demonstrated that the porous Co/C composites are successfully fabricated by the thermal decomposition of the Co-MOF precursors under Ar. As a type of important ferromagnetic metallic materials, various Co nano or microstructures, such as hollow Co spheres, Co nanoflakes, and sword-like Co particles, have been widely used for applications of electromagnetic wave absorption.[32−34] Previous studies have demonstrated that the electromagnetic wave absorption performance of Co nano or microstructures can be promoted by the incorporation of carbon materials.[14−16] Considering the composite constituent and porous architecture, the as-prepared Co/C composites are certainly anticipated to exhibit excellent electromagnetic wave absorption capability.

First, the magnetic properties of Co/C samples were studied at room temperature using a VSM. As shown in Figure 5, all the samples exhibit typical ferromagnetic hysteresis loops, caused by the presence of metallic Co nanoparticles. The saturation magnetization (M_S) of Co/C-500, Co/C-600, and Co/C-800 is 14.5, 64.0, and 80.4 emu g^{-1} (Table 2), respectively, which are all lower than that of bulk Co (164.8 emu g^{-1} at T = 300 K, 155.2 emuvg^{-1} at T = 412 K) but are comparable to that of the Co/C nanocomposites previously reported (58.9 emu·g^{-1}).[14,31,35] The low M_S of the as-prepared Co/C samples is mainly attributed to the formation of CoO on the surface of Co nanoparticles when they are exposed to air. Moreover, the relatively poor crystallinity of the as-prepared Co/C samples is probably another important factor that can induce the enhancement of spin disorder, thereby resulting in low saturation magnetization. Note that the saturation magnetization of Co/C composites tends to rise with elevating calcination temperature; this is mainly because the crystallinity of the samples enhances and the size of the magnetic Co nanoparticles becomes larger with the increase of calcination temperature. In addition, the amount of CoO on the surface of Co also has a minor influence on M_S, because the surface oxidation of Co nanoparticles is virtually impossible to avoid in air. According to the O contents detected in EDX (Table S1 in the Supporting Information), it is roughly deduced that the amount of CoO decreases and the amount of Co increases with increasing temperature of calcination (Table S1). All these factors result in the highest $\mathrm{M_S}$ of Co/C-800. On the other hand, as shown in the corresponding magnified hysteresis loops at low applied magnetic fields (see inset of Figure 5), the coercivity (H_C) values of the Co/C samples vary significantly: 66.1 Oe (Co/C-500), 159.6 Oe (Co/C-600), and 221.6 Oe (Co/C-800). By comparison, the H_C values of the as-prepared Co/C samples are all significantly greater than that of bulk cobalt (10 Oe).[36] The increase of H_C is attributed to the nanometer size of Co particles in the composites because $\mathrm{H_C}$ increases at first and then gradually decreases from the peak value (at critical particle diameter) with increasing size.[37] For Co particles, the critical particle diameter is 70 nm, which is greater than those of Co/C-500 (∼6 nm), Co/C-600 (∼10

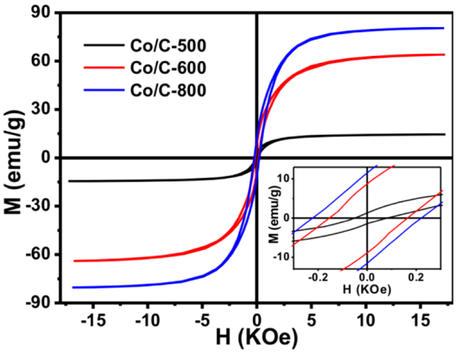

Figure 5. Magnetic hysteresis loops of Co/C-500, Co/C-600, and Co/C-800 at 300 K. Inset shows the corresponding magnified hysteresis loops at low applied magnetic fields.

Table 2. Electromagnetic Wave Absorption Properties of Co/C-500, Co/C-600, and Co/C-800

			electromagnetic wave absorption properties of paraffin wax composites			
samples	H_c (Oe)	M_s (emu g^{-1})	min RL value (dB)	F_m (GHz) (min RL)	d_m (mm) (min RL)	frequency range (GHz) (RL < −10 dB)
Co/C-500	66.1	14.5	−35.0	5.8	4.0	8.4−14.2 (2.5 mm)
Co/C-600	159.6	64.0	−12.0	11.3	1.5	10.6−12.6 (1.5 mm)
Co/C-800	221.6	80.4	−2.8	15.0	1.0	

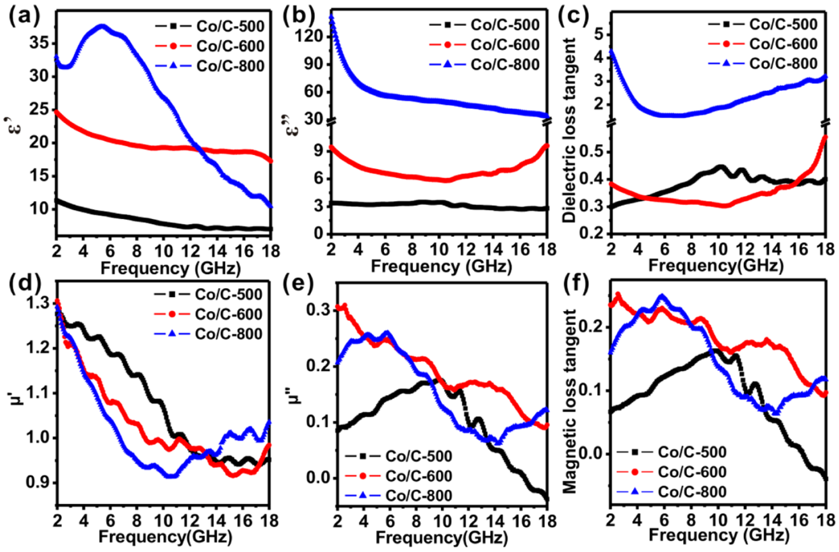

Figure 6. Frequency dependence of electromagnetic parameters of the samples obtained at different temperatures. (a) the real part (ε') and (b) imaginary part (ε'') of complex permittivity, (c) dielectric loss (tan δ_E), (d) real part (μ') and (e) imaginary part (μ'') of complex permeability, (f) magnetic loss (tan δ_M).

nm), and Co/C-800 (~20 nm) and significantly less than that of bulk cobalt.[37]

According to the electromagnetic energy conversion principle,[28] the reflection and attenuation characteristics of electromagnetic wave absorbers are determined by the relative complex permittivity ($\varepsilon_r = \varepsilon' - j\varepsilon''$), relative complex permeability ($\mu_r = \mu' - j\mu''$) and proper matching between complex permittivity and permeability. The real parts (ε' or μ') are related to the stored electrical and magnetic energy within the medium, while the imaginary parts (ε'' and μ'') are related to the dissipation (or loss) of electrical and magnetic energy. The dielectric and magnetic dissipation factors, tan $\delta_E = \varepsilon''/\varepsilon'$ and tan $\delta_M = \mu''/\mu'$, respectively, provide a measure of the power lost in a material versus the amount of power stored.[38−42] Figure 6 shows the frequency dependence of electromagnetic parameters of the wax composites containing 60 wt % Co/C obtained at different temperatures. As shown in Figure 6a, overall, the ε' values of Co/C-500 and Co/C-600 tend to decrease continuously with increasing frequency; the ε' value decreases from 11.35 to 7.04 for Co/C-500 and from 24.68 to 17.29 for Co/C-600. However, the ε' value of Co/C-800 increases at first and then gradually decreases from its peak at 37.70 at 5.39 GHz to 17.91 at 18 GHz, with increasing frequency. As shown in Figure 6b, the ε'' value of Co/C-500 shows marginal fluctuation (~3), and the ε'' value of Co/C-600 shows marginal variation (6.0−9.4). Moreover, unexpectedly, the ε'' value of Co/C-800 ranges from 141.6 to 33.7, which is significantly larger than those of Co/C-500 and Co/C-600. Likewise, tan δ_E of Co/C-800 is greater than those of Co/C-500 and Co/C-600 (Figure 6c). This indicates that Co/C-800, as compared to Co/C-500 and Co/C-600, exhibits higher storage and loss capabilities for electric energy. The permittivity behavior of Co/C-800 can be attributed to the increase of electric conductivity and space-charge polarization among Co particles being efficiently isolated by epoxy resin. Usually, the permittivity values of resin composites increase with increasing loading of metals, which exhibit good electric conductivity.[33] Among the three samples, Co/C-800 exhibits the best electric conductivity because of the best crystallinity of Co particles, which can be deduced by the strong Co XRD peaks (Figure 4a) and the highest M_S (Figure 5). In particular, the porous structure definitely decreases the effective permittivity and benefits impedance match.[43] Co/C-500 and Co/C-600 have an apparent porous structure. When the calcination temperature is increased to 800 °C, most of the rhombic dodecahedral particles become agglomerates (Figure 3c$_{1-3}$). Hence, Co/C-500 and Co/C-600 have the lower effective permittivity and better impedance match.

Figure 6d indicates that the real part (μ') of the complex permeability for the three samples decreases with increasing f value in the range of 2−11 GHz. The decrease in amplitude follows the order of Co/C-800 > Co/C-600 > Co/C-500. Notably, among the three samples, Co/C-500 has the highest μ' at low f, while Co/C-800 has the highest μ' when $f > 13$ GHz. This indicates that Co/C-500, as compared to Co/C-600 and Co/C-800, exhibits higher storage capability for magnetic energy. However, among the three samples, Co/C-600 has the highest μ'' and tan δ_M values, indicating the best dissipation of magnetic energy (Figure 6e, f). When f increases, the imaginary parts (μ'') of the complex permeability for Co/C-600 decreases; however, for Co/C-500 and Co/C-800, μ'' values are maximum. The resonance peak frequencies of Co/C-500 and Co/C-800 correspond to 10.0 and 5.7 GHz, respectively.The matching between the complex permittivity and

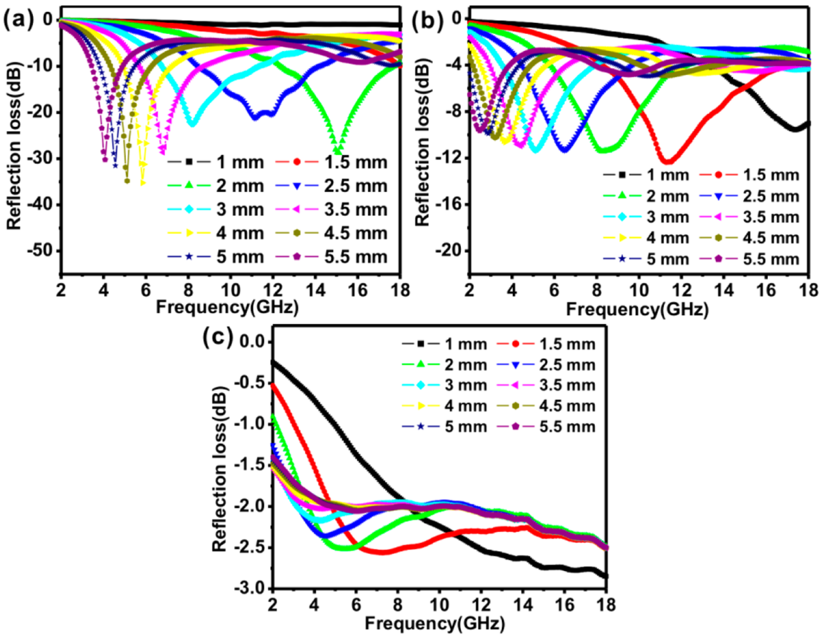

Figure 7. Calculated results of the reflection loss vs frequency for different samples with different thicknesses: (a) Co/C-500, (b) Co/C-600, and (c) Co/C-800 samples.

permeability is mainly reflected in the comparison of the dielectric dissipation factors (tan δ_E) and magnetic dissipation factors (tan δ_M). The difference between tan δ_E and tan δ_M of Co/C-800 is the greatest, but the Co/C-500 has the close value of tan δ_E and tan δ_M, the same as Co/C-600. So Co/C-500 and Co/C-600 exhibit better impedance matching and possess higher loss capabilities for magnetic energy. Therefore, Co/C-500 and Co/C-600 may exhibit the better electromagnetic wave absorption properties (see Table 2). But Co/C-500 exhibits highest storage capability for magnetic energy with the highest μ', and Co/C-500 accordingly exhibits the best electromagnetic wave absorption properties.

To evaluate the electromagnetic wave absorption performance, we calculated the RL values from the relative permeability and permittivity at a given frequency and absorber thickness. Figure 7a−c shows the RL curves of Co/C-500, Co/C-600, and Co/C-800 with specific thickness at 2−18 GHz, respectively. Both Co/C-500 and Co/C-600 exhibit good microwave absorption ability, and the maximum RL obviously shifts to lower frequency with increasing thickness.[44] For Co/C-500, the maximum RL is −35.3 dB at 5.8 GHz with a thickness of 4 mm, which is higher than that reported previously for Co/carbon nanotube composites used as a filler.[14] Noticeably, the RL values below −10 dB, which corresponds to greater than 90% microwave absorption, are achieved in the frequency range of 8.40−14.20 GHz with an absorber thickness of 2.5 mm. This frequency range is wider than the one of porous Co/carbon nanocomposites published in literature (8.0−10.5 GHz).[15] However, the maximum RL of Co/C-600 is only −12.0 dB at 11.3 GHz with a thickness of 1.5 mm, and the frequency corresponding to RL below −10 dB ranges between 10.6 and 12.6 GHz with an absorber thickness of 1.5 mm. In contrast to Co/C-500, for Co/C-600, the bandwidth corresponding to RL below −10 dB obviously shifts to a lower frequency. Among the three samples, Co/C-800 exhibits the worst electromagnetic wave absorption property with the maximum RL less than −3 dB. The similar values of dielectric loss and magnetic loss can lead to the good impedance match of electromagnetic wave absorbing materials.[45−47] Co/C-800 has the highest dielectric loss, which is significantly greater than its magnetic loss value. Therefore, Co/C-800 has a bad impedance match. However, the dielectric loss value and magnetic loss value of Co/C-500 is similar, the same as those for Co/C-600, indicating that Co/C-500 and Co/C-600 have a good impedance match.

As we mentioned, the excellent electromagnetic wave absorption performance of a material requires good impedance match and absorption property, which are associated with complex permittivity, complex permeability, thickness and material structure.[45−47] The Co/C composites can effectively utilize the large magnetic loss of Co and the large dielectric loss value of carbon. Meanwhile, the composites consisting of a carbon matrix have advantages of being lightweight. In Figure 7, the strong absorption peaks of Co/C-500 and Co/C-600 are attributed to resonant absorption at a given frequency and thickness, which should be caused by the "geometrical effect".[44,48] Obviously, porous materials have better impedance match with a free space than corresponding solid materials because of their low effective permittivity.[47] The electromagnetic waves can easily enter into the porous structure and then dissipate in the composites. From SEM observation (Figure 3), Co/C-500 and Co/C-600 maintain a highly porous morphology; however, Co/C-800 consists of agglomerates. In addition, because of the highly porous structure, there are innumerable Co/Co and Co/C interfaces in the Co/C composites. These multi-interfaces result in significant interfacial polarization, which would enhance the dielectric loss obviously.[49] Furthermore, the permeability of Co/C composites could be improved by decreasing the eddy current loss due to the presence of insulating cobalt oxide.[50] Above all, Co/C-500 and Co/C-600, as compared to Co/C-800, have better impedance match with free space because of their low effective permittivity.

4. CONCLUSIONS

In conclusion, we developed a facile route to synthesize highly porous Co/C composites, which is based on the one-step carbonization of the Co-MOF (ZIF-67) precursors under inert atmosphere. Our experiments demonstrated that the as-synthesized porous Co/C composites exhibited excellent electromagnetic wave absorption properties, caused by the synergetic effects between the multiple components and highly porous structure. The maximum RL of Co/C-500, among the three Co/C composites synthesized at different temperatures, reached −35.3 dB at 5.8 GHz with a thickness of 4 mm, and the effective absorption bandwidth (RL ≤ −10 dB) was 5.80 GHz (8.40 GHz−14.20 GHz) corresponding to a thickness of 2.5 mm. Notably, this MOF-derived synthetic method is quite facile, and abundant MOF materials can provide possibilities for fabricating other porous metal/C composites with a wide range of compositions.

■ ASSOCIATED CONTENT

Ⓢ Supporting Information

SEM images and XRD patterns of the products obtained after calcining ZIF-67 at 300 °C for 5 h under different atmospheres (Figure S1), adsorption−desorption isotherms of samples (Figure S2), and EDX results of the products obtained at different temperatures. The Supporting Information is available free of charge on the ACS Publications website at DOI: 10.1021/acsami.5b03177.

■ AUTHOR INFORMATION

Corresponding Author

*E-mail: qkuang@xmu.edu.cn.

Notes

The authors declare no competing financial interest.

■ ACKNOWLEDGMENTS

This work was supported by the National Basic Research Program of China (2011CBA00508), the National Natural Science Foundation of China (21171142, 21473146, and 21333008), and the program for New Century Excellent Talents in University (NCET-11-0294).

■ REFERENCES

(1) Michal, O.; Maria, A. A Study of Handset Antenna and Human Body Interaction. *IEEE Trans. Microwave Theory Technol.* **1996**, *44*, 1855−1864.

(2) Hirata, A.; Matsuyama, S.; Shiozawa, T. Temperature Rises in the Human Eye Exposed to EM Waves in the Frequency Range 0.6−6 GHz. *IEEE Trans. Electromagn. Compat.* **2000**, *42*, 386−393.

(3) Joo, J.; Epstein, A. J. Electromagnetic Radiation Shielding by Intrinsically Conducting Polymers. *Appl. Phys. Lett.* **1994**, *65*, 2278−2280.

(4) Joo, J.; Lee, C. Y. J. High Frequency Electromagnetic Interference Shielding Response of Mixtures and Multilayer Films Based on Conducting Polymers. *Appl. Phys.* **2000**, *88*, 513−518.

(5) Motojima, S.; Noda, Y.; Hoshiya, S.; Hishikawa, Y. Electromagnetic Wave Absorption Property of Carbon Microcoils in 12−110 GHz Region. *J. Appl. Phys.* **2003**, *94*, 2325−2330.

(6) Wang, A.; Wang, W.; Long, C.; Li, W.; Guan, J.; Gu, H.; Xu, G. Facile preparation, Formation Mechanism and Microwave Absorption Properties of Porous Carbonyl Iron Flakes. *J. Mater. Chem. C* **2014**, *2*, 3769−3776.

(7) Huang, X.; Zhang, J.; Lai, M.; Sang, T. Preparation and Microwave Absorption Mechanisms of the NiZn Ferrite Nanofibers. *J. Alloys Compd.* **2015**, *627*, 367−373.

(8) Li, J.; Huang, J.; Qin, Y.; Ma, F. Magnetic and Microwave Properties of Cobalt Nanoplatelets. *Mater. Sci. Eng., B* **2007**, *138*, 199−204.

(9) Tang, X.; Tian, Q.; Zhao, B.; Hu, K. The Microwave Electromagnetic and Absorption Properties of Some Porous Iron Powders. *Mater. Sci. Eng., A* **2007**, *445*, 135−140.

(10) Lu, B.; Dong, X. L.; Huang, H.; Zhang, X. F.; Zhu, X. G.; Lei, J. P.; Sun, J. P. Microwave Absorption Properties of the Core/shell-type Iron and Nickel Nanoparticles. *J. Magn. Magn. Mater.* **2008**, *320*, 1106−1111.

(11) Yang, Y.; Xu, C.; Xia, Y.; Wang, T.; Li, F. Synthesis and Microwave Absorption Properties of FeCo Nanoplates. *J. Alloys Compd.* **2010**, *493*, 549−552.

(12) Chen, Z.; Xu, C.; Ma, C.; Ren, W.; Cheng, H. M. Lightweight and Flexible Graphene Foam Composites for High-Performance Electromagnetic Interference Shielding. *Adv. Mater.* **2013**, *25*, 1296−300.

(13) Wen, B.; Cao, M.; Lu, M.; Cao, W.; Shi, H.; Liu, J.; Wang, X.; Jin, H.; Fang, X.; Wang, W.; Yuan, J. Reduced Graphene Oxides: Light-Weight and High-Efficiency Electromagnetic Interference Shielding at Elevated Temperatures. *Adv. Mater.* **2014**, *26*, 3484−3489.

(14) Yi, H. B.; Wen, F. S.; Qiao, L.; Li, F. S. Microwave Electromagnetic Properties of Multiwalled Carbon Nanotubes Filled with Co Nanoparticles. *J. Appl. Phys.* **2009**, *106*, 103922.

(15) Liu, Q. L.; Zhang, D.; Fan, T. X. Electromagnetic Wave Absorption Properties of Porous Carbon/Co Nanocomposites. *Appl. Phys. Lett.* **2008**, *93*, 013110.

(16) Sui, J. H.; Zhang, C.; Li, J.; Yu, Z. L.; Cai, W. Microwave Absorption and Catalytic Activity of Carbon Nanotubes Decorated with Cobalt Nanoparticles. *Mater. Lett.* **2012**, *75*, 158−160.

(17) Zhang, H.; Zhang, J.; Zhang, H. Computation of Radar Absorbing Silicon Carbide Foams and Their Silica Matrix Composites. *Comput. Mater. Sci.* **2007**, *38*, 857−864.

(18) Zhou, J.; He, J.; Li, G.; Wang, T.; Sun, D.; Ding, X.; Zhao, J.; Wu, S. Direct Incorporation of Magnetic Constituents within Ordered Mesoporous Carbon-Silica Nanocomposites for Highly Efficient Electromagnetic Wave Absorbers. *J. Phys. Chem. C* **2010**, *114*, 7611−7617.

(19) Kim, S. S.; Kim, S. T.; Ahn, J. M.; Kim, K. H. Magnetic and Microwave Absorbing Properties of Co−Fe Thin Films Plated on Hollow Ceramic Microspheres of Low Density. *J. Magn. Magn. Mater.* **2004**, *271*, 39−45.

(20) Chen, Y. J.; Xiao, G.; Wang, T. S.; Ouyang, Q. Y.; Qi, L. H.; Ma, Y.; Gao, P.; Zhu, C. L.; Cao, M. S.; Jin, H. B. Porous Fe3O4/Carbon Core/Shell Nanorods: Synthesis and Electromagnetic Properties. *J. Phys. Chem. C* **2011**, *115*, 13603−13608.

(21) Sun, J. K.; Xu, Q. Functional Materials Derived from Open Framework Templates/Precursors: Synthesis and Applications. *Energy Environ. Sci.* **2014**, *7*, 2071−2100.

(22) Benjamin, W.; Ronald, J. T.; Mitchell, R.; Stephen, D.; Ian, M.; Alec, T. A.; Mark, D. Ordered Metal Nanostructure Self-assembly Using Metal−Organic Frameworks as Templates. *Chem. Sci.* **2011**, *2*, 411−416.

(23) Peng, L.; Zhang, J.; Xue, Z.; Han, B.; Li, J.; Yang, G. Large-pore Mesoporous Mn3O4 Crystals Derived from Metal-Organic Frameworks. *Chem. Commun.* **2013**, *49*, 11695−11697.

(24) Gai, P. B.; Zhang, H. J.; Zhang, Y. S.; Liu, W.; Zhu, G. B.; Zhang, X. H.; Chen, J. H. Simultaneous Electrochemical Detection of Ascorbic Acid, Dopamine and Uric Acid Based on Nitrogen Doped Porous Carbon Nanopolyhedra. *J. Mater. Chem. B* **2013**, *1*, 2742−2749.

(25) deKrafft, K. E.; Wang, C.; Lin, W. Metal-Organic Framework Templated Synthesis of Fe2O3/TiO2 Nanocomposite for Hydrogen Production. *Adv. Mater.* **2012**, *24*, 2014−2018.

(26) Liu, B.; Shioyama, H.; Akita, T.; Xu, Q. Metal-Organic Framework as a Template for Porous Carbon Synthesis. *J. Am. Chem. Soc.* **2008**, *130*, 5390−5391.

(27) Jiang, Z.; Li, Z.; Qin, Z.; Sun, H.; Jiao, X.; Chen, D. LDH Nanocages Synthesized with MOF Templates and Their High Performance as Supercapacitors. *Nanoscale* **2013**, *5*, 11770−11775.

(28) Toru, M.; Satoshi, S.; Toshio, K.; Nobuki, T.; Koichiro, I. Effect of the Soft/Hard Exchange Interaction on Natural Resonance Frequency and Electromagnetic Wave Absorption of the Rare

Earth−Iron−Boron Compounds. *J. Magn. Magn. Mater.* **2004**, *281*, 195−205.

(29) Lu, Y.; Zhan, W.; He, Y.; Wang, Y.; Kong, X.; Kuang, Q.; Xie, Z.; Zheng, L. MOF-Templated Synthesis of Porous Co3O4 Concave Nanocubes with High Specific Surface Area and Their Gas Sensing Properties. *ACS Appl. Mater. Interfaces* **2014**, *6*, 4186−4195.

(30) Wang, Z. H.; Xiong, X. Q.; Qie, L.; Huang, Y. H. High-Performance Lithium Storage in Nitrogen-Enriched Carbon Nanofiber Webs Derived from Polypyrrole. *Electrochim. Acta* **2013**, *106*, 320−326.

(31) Torad, N. L.; Hu, M.; Ishihara, S.; Sukegawa, H.; Belik, A. A.; Imura, M.; Ariga, K.; Sakka, Y.; Yamauchi, Y. Direct Synthesis of MOF-Derived Nanoporous Carbon with Magnetic Co Nanoparticles toward Efficient Water Treatment. *Small* **2014**, *10*, 2096−2107.

(32) Ma, F.; Qin, Y.; Li, Y. Z. Enhanced Microwave Performance of Cobalt Nanoflakes with Strong Shape Anisotropy. *Appl. Phys. Lett.* **2010**, *96*, 202507.

(33) He, C. Z.; Qiu, S.; Wang, X. Z.; Liu, J. R.; Luan, L. Q.; Liu, W.; Itoh, M.; Machida, K. Facile Synthesis of Hollow Porous Cobalt Spheres and Their Enhanced Electromagnetic Properties. *J. Mater. Chem.* **2012**, *22*, 22160−22166.

(34) Wen, S. L.; Zhao, X. C.; Liu, Y.; Cheng, J. W.; Li, H. Synthesis of Hierarchical Sword-Like Cobalt Particles and Their Microwave Absorption Properties. *RSC Adv.* **2014**, *4*, 40456−40463.

(35) García Prieto, A.; Fdez-Gubieda, M.; Meneghini, C.; García-Arribas, A.; Mobilio, S. Microstructural and Magnetic Evolution upon Annealing of Giant Magnetoresistance Melt-Spun Co-Cu Granular Alloys. *Phys. Rev. B* **2003**, *67*, 224415.

(36) Zhang, Y.; Yao, Q.; Zhang, Y.; Cui, T.; Li, D.; Liu, W.; Lawrence, W.; Zhang, Z. Solvothermal Synthesis of Magnetic Chains Self-Assembled by Flowerlike Cobalt Submicrospheres. *Cryst. Growth Des.* **2008**, *8*, 3206−3212.

(37) Leslie-Pelecky, D. L.; Rieke, R. D. Magnetic Properties of Nanostructured Materials. *Chem. Mater.* **1996**, *8*, 1770−1783.

(38) Fan, Z.; Luo, G.; Zhang, Z.; Zhou, L.; Wei, F. Electromagnetic and Microwave Absorbing Properties of Multi-Walled Carbon Nanotubes/Polymer Composites. *Mater. Sci. Eng., B* **2006**, *132*, 85−89.

(39) Su, Q.; Li, J.; Zhong, G.; Du, G.; Xu, B. In Situ Synthesis of Iron/Nickel Sulfide Nanostructures-Filled Carbon Nanotubes and Their Electromagnetic and Microwave-Absorbing Properties. *J. Phys. Chem. C* **2011**, *115*, 1838−1842.

(40) Zhao, D.; Li, X.; Shen, Z. Microwave Absorbing Property and Complex Permittivity and Permeability of Epoxy Composites Containing Ni-Coated and Ag Filled Carbon Nanotubes. *Compos. Sci. Technol.* **2008**, *68*, 2902−2908.

(41) Li, G.; Xie, T.; Yang, S.; Jin, J.; Jiang, J. Microwave Absorption Enhancement of Porous Carbon Fibers Compared with Carbon Nanofibers. *J. Phys. Chem. C* **2012**, *116*, 9196−9201.

(42) Qing, Y.; Zhou, W.; Luo, F.; Zhu, D. Microwave-Absorbing and Mechanical Properties of Carbonyl-iron/Epoxy-silicone Resin Coatings. *J. Magn. Magn. Mater.* **2009**, *321*, 25−28.

(43) Li, X.; Zhang, B.; Ju, C.; Han, X.; Du, Y.; Xu, P. Morphology-Controlled Synthesis and Electromagnetic Properties of Porous Fe3O4 Nanostructures from Iron Alkoxide Precursors. *J. Phys. Chem. C* **2011**, *115*, 12350−12357.

(44) Yusoff, A. N.; Abdullah, M. H.; Ahmad, S. H.; Jusoh, S. F.; Mansor, A. A.; Hamid, S. A. A. Electromagnetic and Absorption Properties of Some Microwave Absorbers. *J. Appl. Phys.* **2002**, *92*, 876−882.

(45) Ma, Z.; Zhang, Y.; Cao, C.; Yuan, J.; Liu, Q.; Wang, J. Attractive Microwave Absorption and the Impedance Match Effect in Zinc Oxide and Carbonyl Iron Composite. *Phys. B (Amsterdam, Neth.)* **2011**, *406*, 4620−4624.

(46) Li, G.; Wang, L.; Li, W.; Ding, R.; Xu, Y. CoFe2O4 and/or Co3Fe7 Loaded Porous Activated Carbon Balls as a Lightweight Microwave Absorbent. *Phys. Chem. Chem. Phys.* **2014**, *16*, 12385−12392.

(47) Wang, B.; Zhang, J.; Wang, T.; Qiao, L.; Li, F. Synthesis and Enhanced Microwave Absorption Properties of Ni@Ni2O3 Core−Shell Particles. *J. Alloys Compd.* **2013**, *567*, 21−25.

(48) Fang, Z.; Li, C.; Sun, J.; Zhang, H.; Zhang, J. The Electromagnetic Characteristics of Carbon Foams. *Carbon* **2007**, *45*, 2873−2879.

(49) Sun, D.; Zou, Q.; Wang, Y.; Wang, Y.; Jiang, W.; Li, F. Controllable Synthesis of Porous Fe_3O_4@ZnO Sphere Decorated Graphene for Extraordinary Electromagnetic Wave Absorption. *Nanoscale* **2014**, *6*, 6557−6562.

(50) Wang, Z.; Bi, H.; Wang, P.; Wang, M.; Liu, Z.; Shen, L.; Liu, X. Magnetic and Microwave Absorption Properties of Self-Assemblies Composed of Core−Shell Cobalt−Cobalt Oxide Nanocrystals. *Phys. Chem. Chem. Phys.* **2015**, *17*, 3796.